Spike-adding in a canonical three time scale model: superslow explosion & folded-saddle canards

Mathieu Desroches* Vivien Kirk†

August 12, 2017

Abstract

We examine the origin of complex bursting oscillations in a phenomenological ordinary differential equation model with three time scales. We show that bursting solutions in this model arise from a Hopf bifurcation followed by a sequence of spike-adding transitions, in a manner reminiscent of spike-adding transitions previously observed in systems with two time scales. However, the details of the process can be much more complex in this three-time-scale context than in two-time-scale systems. In particular, we find that spike-adding can involve canard explosions occurring on two different time scales and is associated with passage near a folded-saddle singularity. We show that the form of spike-adding transition that occurs depends on the geometry of certain singular limit systems, specifically the relative positions of the critical and superslow manifolds. We also show that, unlike the case of spike-adding in two-time-scale systems, the onset of a new spike in our model is not typically associated with a local maximum in the period of the bursting oscillation.

1 Introduction

Many natural systems are known to exhibit multiple time scales, that is, they have the property that one or more processes in the system evolve much faster than other processes. A great deal is known about typical behaviour in systems with two time scales, with phenomena such as relaxation oscillations, mixed mode oscillations, and bursting being seen in a wide range of models; see, for example, [1, 2, 15, 18]. However, much less is known about typical dynamics for systems with three or more time scales, despite some recent work [20, 22, 26, 31].

In this article, we are interested in explaining the origin of complex bursting dynamics observed in a particular ordinary differential equation model with three time scales. The model was first constructed by Nan [25] to provide a system whose solutions mimic the complex oscillations seen in the Rosenzweig-MacArthur food chain model [3, 4, 5, 28]. It is a minimal model, in the sense that

*MathNeuro Team, Inria Sophia Antipolis Méditerranée, 2004 route des Lucioles - BP93, 06902 Sophia Antipolis cedex, France, mathieu.desroches@inria.fr.

†Department of Mathematics, University of Auckland, Private Bag 92019 Auckland, New Zealand, v.kirk@auckland.ac.nz.

it has the minimum dimension and simplest nonlinearities consistent with the behaviour of interest, and has the advantage that it is easier to manipulate than the food chain model, to move certain geometric features associated with the model relative to one another. Our interest in this model arises for two reasons. First, we wish to understand the mechanisms underlying the distinctive patterns of oscillation observed by Nan in the model, and in particular to illuminate how different time scales in the model interact to produce the complex dynamics. Second, the way in which the model is parametrised makes it an ideal set-up in which to investigate more general features of three-time-scale dynamics; while our main concern in this paper is to explain the dynamics of the model in a certain parameter regime, we believe that a thorough understanding of the model dynamics for different values of the system parameters will have a much wider relevance, and in particular will contribute to overall understanding of the difference between models with two time scales and with those with three time scales.

The model we consider takes the form [25]:

$$\begin{aligned}
\frac{dx}{dt} &= y - \left(a_3x^3 - a_2x^2 + a_1x + a_0\right) \;:=\; f(x,y) \\
\frac{dy}{dt} &= \delta(b_2x^2 - b_1x - c_1y - z + c_0) \;:=\; \delta g(x,y,z) \\
\frac{dz}{dt} &= \delta\varepsilon(x - \gamma) \;:=\; \delta\varepsilon h(x),
\end{aligned} \tag{1}$$

where $x, y, z \in \mathbb{R}$. The constants δ and ε control the time scale separation in the model dynamics, as will be explained further below; we always consider small non-negative values of these constants, usually $\delta = 0.001$ and $\varepsilon = 0.1$. The parameter γ is the main bifurcation parameter in our model; we consider $\gamma \in [0, 1]$. We follow Nan [25] in our choice of the other parameter values and, unless otherwise stated, these are set to the values specified in Table 1.

Table 1: Default values for the parameters in model (1).

a_0	0.1	a_1	1.56
a_2	5.1	a_3	4.0
b_1	80.25	b_2	60.0
c_0	27.75	c_1	12.5
δ	0.001	ε	0.1

We note that an alternative way of parametrising our system, with the various coefficients expressed in terms of other constants, is given in Appendix A. The alternative form is useful for the manipulation of certain geometric features of the model, as will be discussed further in Sections 4 and 5.

For the choice $\gamma = 0.92$, system (1) has the attracting periodic solution shown in Fig. 1. Different time scales are evident in the time series: there appears to be a two-time-scale relaxation oscillation in the x and y variables, and a rise and fall in z over a slower, third time scale. The dynamics bears some resemblance to bursting oscillations typically seen in the Hindmarsh-Rose model [14] and many similar systems [15, 27], but the spikes during the bursts in

the Hindmarsh-Rose model are not usually relaxation oscillations, a reflection of that model having only two time scales.

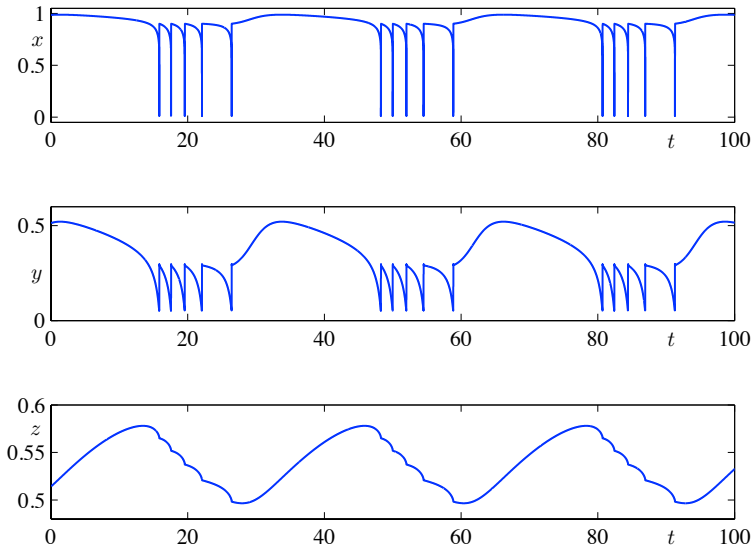

Figure 1: Time series showing an attracting oscillation for system (1) with $\gamma = 0.92$ and other parameters as in Table 1.

The time series in Fig. 1 shows that there are five sharp spikes in the amplitude of x and y during each burst, but, as we shall show below, varying γ can result in spikes being added or removed from the bursts. Spike-adding in bursting systems with two time scales has been extensively studied [7, 8, 12, 27, 30]. A primary aim in this paper is to examine the spike-adding process in our three-time-scale system and to show that there are important differences to the spike-adding seen in two-time-scale systems. In particular, we observe some features in the spike-adding process that are similar to those seen in systems of Hindmarsh-Rose type (with two time scales and one slow variable) and some features that are similar to spike-adding seen in systems with parabolic bursting (with two time scales and two slow variables).

This paper is organised as follows. In Section 2, we summarise ideas from geometric singular perturbation theory (GSPT) that we will use subsequently to explain the dynamics of our model. In Section 3 we give an overview of the dynamics of the model as the parameter γ is varied, with results obtained from numerical simulation and continuation of the model. In Section 4 we examine spike adding in the model in detail, both in a parameter regime in which all three time scales are crucial to the transition associated with addition of a single spike and in a parameter regime where only two time scales make a contribution to spike adding. In Section 5, we summarise our results and their relationship to results from earlier work in the literature, and make some comments about possible extensions of our work.

2 Preliminary analysis

In our analysis of system (1), we will exploit the presence of different time scales to enable us to use methods from GSPT [11, 16, 19] and blow-up theory [10, 19, 29, 32]. We are interested mostly in the positive octant of phase space with $x, y, z < 1$. In this regime, the functions f, g and h defined in (1) are all approximately $O(1)$, meaning that the right-hand sides of the three equations in (1) are approximately $O(1)$, $O(\delta)$ and $O(\delta\varepsilon)$, respectively. For sufficiently small δ and ε, we can therefore regard these variables as evolving on three different time scales: we say that x is a fast variable, y is slow and z is superslow. Thus, δ can be regarded as encoding the separation between the fast and slow time scales, and ε represents the separation between the slow and superslow time scales. For the purposes of this article, we are primarily interested in explaining the dynamics observed when $\delta = 0.001$ and $\varepsilon = 0.1$; similar dynamics persists more generally for $0 < \delta \ll \varepsilon \ll 1$. As will be seen, this choice of the relative sizes of δ and ε allows us to make some progress by treating the system as a two-time-scale system (with one fast and two slow variables), but we start out by defining subsystems and singular limits appropriate to a three-time-scale context.

Following standard methods from GSPT, we define equivalent versions of our model using different time scales. System (1) is written using (fast) time, t, and is called the *fast system*. Defining $t_s = \delta t$, we get the *slow system*,

$$\begin{aligned} \delta\frac{dx}{dt_s} &= f(x,y) \\ \frac{dy}{dt_s} &= g(x,y,z) \\ \frac{dz}{dt_s} &= \varepsilon h(x), \end{aligned} \tag{2}$$

where f, g and h are as defined for system (1). Defining $t_{ss} = \varepsilon t_s = \varepsilon\delta t$, we get the *superslow system*,

$$\begin{aligned} \varepsilon\delta\frac{dx}{dt_{ss}} &= f(x,y) \\ \varepsilon\frac{dy}{dt_{ss}} &= g(x,y,z) \\ \frac{dz}{dt_{ss}} &= h(x). \end{aligned} \tag{3}$$

These three versions of the model are equivalent if $\varepsilon \neq 0$ and $\delta \neq 0$, but they produce non-equivalent systems when we take singular limits by letting one or both of ε and δ tend to zero. Throughout the present work, we will assume $\delta \ll \varepsilon$, and therefore consider either the ε-dependent singular limit obtained by letting $\delta \to 0$ with $\varepsilon > 0$ fixed or the double singular limit obtained by letting $\delta \to 0$ while ε is fixed then letting $\varepsilon \to 0$.

Letting $\delta \to 0$ in (1) yields the *fast layer problem*,

$$\begin{aligned} \frac{dx}{dt} &= f(x,y) \\ \frac{dy}{dt} &= 0 \\ \frac{dz}{dt} &= 0. \end{aligned} \tag{4}$$

Thus, in the fast layer problem, the fast variable, x, evolves along one-dimensional *fast fibres* defined by $(x,y,z) = (x,y_0,z_0)$ for constants y_0 and z_0. The two-dimensional set of equilibria of (4),

$$S_0 = \{(x,y,z) \mid f(x,y) = 0\},$$

is called the *critical manifold*. For our choice of f, the critical manifold is

$$S_0 = \{(x,y,z) \mid y = a_3x^3 - a_2x^2 + a_1x + a_0\},$$

and is a surface that is folded with respect to y, as shown in Fig. 2; the lines of folds are labelled L^- and L^+ in Fig. 2, and occur at $x = 0.20$ and $x = 0.65$ for the parameter values in Table 1. The folds divide S_0 into attracting and repelling sheets; the inner sheet, lying between the two fold curves, is repelling since, in the fast layer problem, the corresponding equilibria are repelling, and the two outer sheets are attracting.

A different singular limit system is obtained by letting $\delta \to 0$ in the slow system (2). This yields the differential-algebraic *slow reduced problem*

$$\begin{aligned} 0 &= f(x,y) \\ \frac{dy}{dt_s} &= g(x,y,z) \\ \frac{dz}{dt_s} &= \varepsilon h(x), \end{aligned} \tag{5}$$

which describes the dynamics restricted to S_0. For ε sufficiently small, this is a two-time-scale problem. Letting $\varepsilon \to 0$ in (5) gives the *slow layer problem*,

$$\begin{aligned} 0 &= f(x,y) \\ \frac{dy}{dt_s} &= g(x,y,z) \\ \frac{dz}{dt_s} &= 0. \end{aligned} \tag{6}$$

Thus, in the slow layer problem, the slow variable, y, evolves along one-dimensional fibres defined by $(x,y,z) = (x,y,z_0)$, for constant z_0 and for (x,y,z_0) restricted to S_0. The one-dimensional set of equilibria of (6),

$$\mathscr{S}_0 = \{(x,y,z) \mid f(x,y) = 0 \text{ and } g(x,y,z) = 0\},$$

is called the *superslow manifold*. For our choice of f and g, the superslow manifold is

$$\mathscr{S}_0 = \{(x,y,z) \mid z = -c_1a_3x^3 + (c_1a_2 + b_2)x^2 - (c_1a_1 + b_1)x + c_0 - c_1a_0\},$$

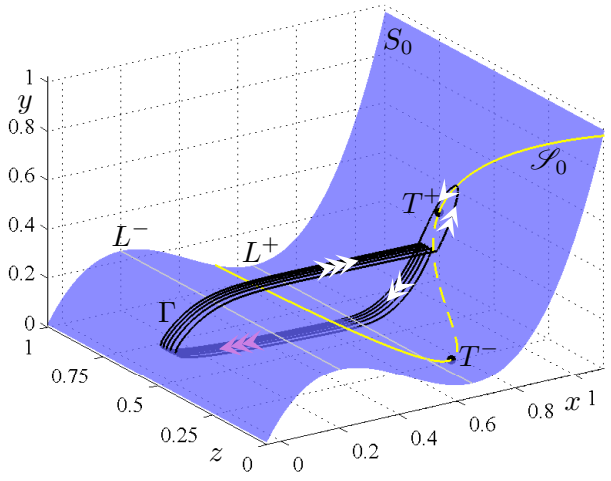

Figure 2: The critical manifold, S_0 (blue surface), and superslow manifold, $\mathscr{S}_0$ (yellow curve), for system (1) with parameter values as in Table 1. The solid (resp. dashed) sections of the yellow curve indicate the segments of $\mathscr{S}_0$ that are attracting (resp. repelling) within the slow layer problem, system (6). The lines labeled L^- and L^+ mark the folds of S_0 relative to y. The points labeled T^- and T^+ mark the folds of $\mathscr{S}_0$ relative to z. Note that the locations of S_0 and $\mathscr{S}_0$ are independent of the bifurcation parameter γ. Also shown is a stable bursting cycle, Γ, obtained by direct simulation of system (1) for $\gamma = 0.92$. The single-headed arrows (resp. double- and triple-headed arrows) indicate orbit segments where the evolution is on the superslow (resp. slow and fast) time scale.

and is a curve that is folded with respect to z, as shown in Fig. 2; the fold points are labelled T^- and T^+ in Fig. 2, and occur at $x = 0.70$ and $x = 0.95$ for the parameter values in Table 1. T^- and T^+ divide $\mathscr{S}_0$ into branches that are attracting and repelling relative to the dynamics restricted to S_0; the inner branch, lying between T^- and T^+, is repelling and the two outer branches are attracting (within S_0).

For completeness, we define one further system, the *superslow reduced problem*, which is obtained by letting $\varepsilon \to 0$ in (3), to yield

$$\begin{aligned} 0 &= f(x,y) \\ 0 &= g(x,y,z) \\ \frac{dz}{dt_{ss}} &= h(x). \end{aligned} \tag{7}$$

This system determines the dynamics restricted to $\mathscr{S}_0$. In our case, since h is so simple, we easily see that the z-coordinate increases if $x > \gamma$ and decreases if $x < \gamma$; this is true both for the dynamics on $\mathscr{S}_0$ and also, more generally, in the full phase space.

To understand the dynamics of our system, it is useful to look more closely at the dynamics restricted to S_0. Using standard ideas from GSPT, we calculate

the projection of the slow reduced flow, equations (5), onto the (x, z) plane. Specifically, since $f(x, y) = 0$ on S_0, differentiating with respect to t_s gives

$$f_y \frac{dy}{dt_s} = -f_x \frac{dx}{dt_s}.$$

Since S_0 can be expressed as $y = F(x)$ for some function F, we can rearrange the equations in (5) to get

$$\begin{aligned} -f_x \frac{dx}{dt_s} &= f_y \, g(x, F(x), z) \\ \frac{dz}{dt_s} &= \varepsilon h(x), \end{aligned} \tag{8}$$

Rescaling time so that $t_s = (-f_x)\tau$ allows us to remove the singularities that occur in (8) when $f_x = 0$ (which occurs on the fold lines L^- and L^+). We then obtain the *desingularised slow reduced system* (DSRS),

$$\begin{aligned} \frac{dx}{d\tau} &= f_y \, g(x, F(x), z) \\ \frac{dz}{d\tau} &= -\varepsilon f_x h(x). \end{aligned} \tag{9}$$

Note that, since $-f_x$ is positive on the attracting sheets of S_0 and negative on the repelling sheet, orbits of (9) corresponding to motion on the repelling sheet of S_0 have a reversed direction of time relative to orbits in the slow reduced system (5) (as well as in its projected version (8)). Using the specific f, g, and h associated with (1), system (9) becomes

$$\begin{aligned} \frac{dx}{d\tau} &= -c_1 a_3 x^3 + (b_2 + c_1 a_2)x^2 - (b_1 + c_1 a_1)x + (c_0 - c_1 a_0) - z \\ \frac{dz}{d\tau} &= \varepsilon(x - \gamma)(3a_3 x^2 - 2a_2 x + a_1). \end{aligned} \tag{10}$$

For ε sufficiently small, system (9) is a two-time-scale system, with time scale separation proportional to ε. After rewriting system (9) in terms of its associated slow time $\tilde{\tau} = \varepsilon\tau$, we can use the singular limit $\varepsilon \to 0$ to reduce and desingularise again, following a similar procedure to that above. Doing so yields an equation for the desingularised version of the dynamics on $\mathscr{S}_0$ projected onto the x-axis:

$$\frac{dx}{d\hat{\tau}} = -g_z f_x h(x), \tag{11}$$

where $\tilde{\tau} = -(g_x + F_x)\hat{\tau}$. Orbits of (11) corresponding to motion on the repelling branch of $\mathscr{S}_0$ have a reversed direction of time relative to orbits of (9). For our choice of parameters, the repelling branch of $\mathscr{S}_0$ is contained entirely within an attracting sheet of S_0, so there is no further sign change relative to the dynamics in the full system. Consideration of this version of the dynamics provides information about the behaviour of solutions following an attracting branch of $\mathscr{S}_0$ as they approach a fold of $\mathscr{S}_0$, as will be explained further below. Using the specific f, g and h associated with (1), system (11) becomes

$$\frac{dz}{d\hat{\tau}} = -(x - \gamma)(3a_3 x^2 - 2a_2 x + a_1). \tag{12}$$

The dynamics of the full system near the attracting sheets of S_0 and near the attracting branches of $\mathscr{S}_0$ can be understood using the various singular limit systems defined above and ideas from GSPT. A fundamental idea is that of *normal hyperbolicity* of the critical and superslow manifolds. In particular, fixing ε and thinking of δ as a small positive constant, S_0 is said to be normally hyperbolic at a particular point if the Jacobian of the fast layer problem (4) evaluated at that point has no eigenvalues with zero real part. In our case, S_0 is normally hyperbolic except on the fold curves, L^+ and L^-. Then Fenichel theory guarantees the persistence of smooth manifolds close to each of the three sheets of S_0, with dynamics on those manifolds being a smooth perturbation of the dynamics on S_0 within the slow reduced problem (5). Similarly, since ε is small, the dynamics on S_0 is itself a two-time-scale problem; letting $\varepsilon \to 0$, we find that $\mathscr{S}_0$ is normally hyperbolic with respect to the slow reduced problem except at its turning points, T^+ and T^-. Fenichel theory then guarantees the persistence of smooth manifolds close to each of the three branches of $\mathscr{S}_0$, with the dynamics on those manifolds being a smooth perturbation of the dynamics on $\mathscr{S}_0$ within (5).

The dynamics near points at which S_0 is not normally hyperbolic can be recovered using blow-up theory [10, 19, 29, 32]. In particular, the attracting and repelling slow manifolds may intersect in the vicinity of non-hyperbolic regions of the critical manifold; such intersections correspond to *canard trajectories*, which will be important for understanding spike adding in our system. Also of interest are *folded singularities*, that is, equilibria of the DSRS that are not equilibria of (8). Folded singularities correspond to points of the slow flow where many trajectories can cross in finite time from an attracting to a repelling sheet of S_0; trajectories crossing through a folded singularity are by definition (singular) canards. Folded singularities of saddle type will turn out to be crucial to our explanation of the dynamics of system (1). Such folded singularities have two special canard solutions, a *true canard* and a *faux canard*, associated with the stable and unstable manifolds of the saddle equilibrium in the DSRS, and we will discuss these more in later sections; see [6] for background material about folded singularities. It is straightforward to show that folded singularities of (9) must satisfy the conditions

$$\begin{aligned} f_x &= 0 \\ f_y g(x, F(x), z) &= 0. \end{aligned} \tag{13}$$

Similarly, the dynamics near points at which $\mathscr{S}_0$ is not normally hyperbolic can be deduced using blow-up theory. In the limit $\varepsilon \to 0$, equilibria of (11) that occur at turning points of $\mathscr{S}_0$ give rise to so-called *canard points*, which are the analogue of folded singularities for the case where the relevant critical manifolds are one dimensional; these points occur near parameter values where the one-dimensional attracting and repelling manifolds (that arise as perturbations of the branches of $\mathscr{S}_0$) coincide, and are associated with the existence of canard trajectories.

Both canard points and folded singularities (at least near so-called *folded-saddle-node singularity of type II*) can be associated with the occurrence of *canard cycles*, which are periodic orbits that contain segments from canard trajectories. From a bifurcation theory perspective, canard cycles are born at so-called *singular Hopf bifurcations* [13], which are characterised by rapid growth

in amplitude of the periodic orbits, giving near-vertical branches of periodic orbits in the bifurcation diagram [6].

Application of standard GSPT now allows us to make some general statements about the dynamics of (1). For sufficiently small δ and ε, an orbit of the full system will typically follow closely an attracting sheet (or branch) of S_0 (or $\mathscr{S}_0$) until it reaches a fold of S_0 (or $\mathscr{S}_0$). Then it will either make a jump on a faster time scale to a different attracting sheet (or branch) of S_0 (or $\mathscr{S}_0$) or start a canard segment, during which it follows a repelling sheet (or branch) of S_0 (or $\mathscr{S}_0$). The orbit typically will leave the repelling sheet or branch eventually and make a transition on a faster time scale to one of the attracting sheets or branches. In this way, an orbit of the full system can be understood as being a perturbation of a sequence of orbit segments from either the slow reduced flow or the superslow reduced flow, interspersed with orbit segments from the fast or slow layer problems.

3 Overview of the model dynamics

Computation using the software package AUTO [9] yields the partial bifurcation diagram for system (1) shown in Fig. 3(a). For each value of the parameter γ there is a single equilibrium solution. The branch of equilibria changes stability at the Hopf bifurcations marked HB_1, HB_2, HB_3 and HB_4. The branches of periodic solutions arising from HB_1 and HB_2 terminate in homoclinic bifurcations of the equilibrium at $\gamma \approx 0.90$ (Hom_1) and $\gamma \approx 0.76$ (Hom_2), respectively; phase portraits for periodic orbits on these branches close to the homoclinic bifurcations are shown in Fig. 3, panels (b) and (c).

The branch of periodic solutions bifurcating from HB_3 terminates in a homoclinic bifurcation of a periodic orbit at the point marked HPo. The time series and phase portrait for a periodic orbit on the branch starting at HB_3, for γ very close to its value at HPo, is shown in Fig. 3, panels (d) (black curve) and (e). Also shown in panel (d) (red curve) is the periodic orbit on the branch arising from HB_2 at the same γ value; it is this periodic orbit that is undergoing the homoclinic bifurcation at HPo.

The branch of periodic orbits arising from HB_4 undergoes a complex series of transitions before ending in a homoclinic bifurcation of an equilibrium at $\gamma \approx 0.90$; an enlargement of this branch is shown in Fig. 3(f), where the homoclinic bifurcation terminating the branch is labelled Hom_4. The precise sequence of changes that occurs along this last branch is the main focus of Section 4.1.

A deeper understanding of the bifurcations shown in Fig. 3(a) can be gained by considering the dynamics of system (10), the desingularised slow reduced system. Recall that these equations approximate the dynamics on S_0 in the limit $\delta \to 0$. There are two types of equilibria of this system. So-called *ordinary singularities* occur at

$$x_o = \gamma, \quad z_o = -c_1 a_3 \gamma^3 + (b_2 + c_1 a_2)\gamma^2 - (b_1 + c_1 a_1)\gamma + (c_0 - c_1 a_0).$$

These correspond to true singularities of (1), and occur at the points at which the z-nullcline (i.e., the plane $x = \gamma$) cuts $\mathscr{S}_0$ for each choice of γ. In addition there are two branches of *folded singularities*, with x-coordinates given by

$$x_{L^+} = \frac{a_2 + \sqrt{a_2^2 - 3a_1 a_3}}{3a_3} \quad \text{and} \quad x_{L^-} = \frac{a_2 - \sqrt{a_2^2 - 3a_1 a_3}}{3a_3}$$

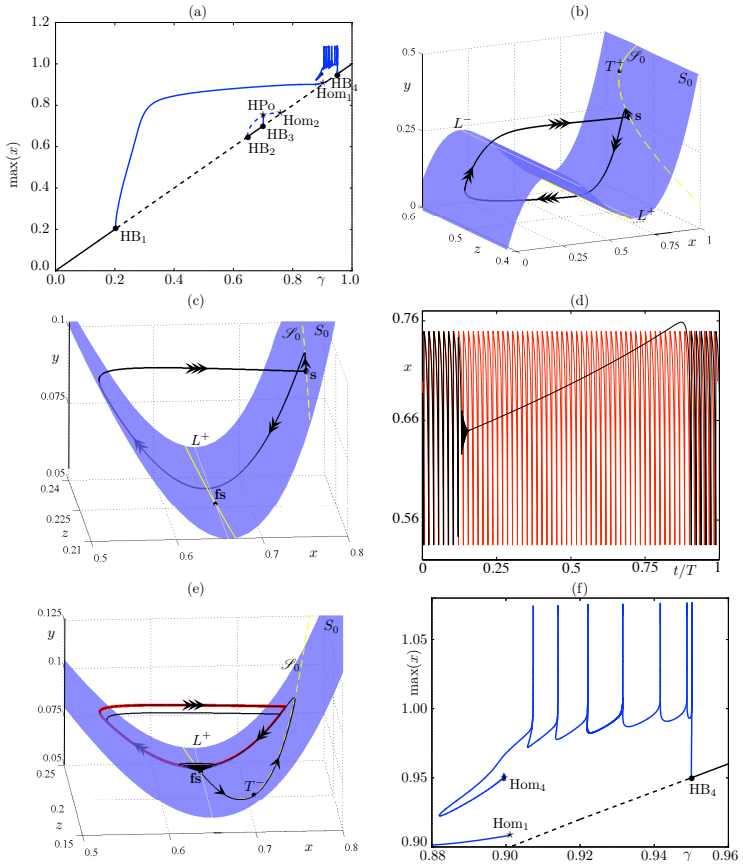

Figure 3: (a) Partial bifurcation diagram of (1), showing equilibria and periodic solutions for $\gamma \in [0, 1]$. The black curve shows equilibrium solutions (solid for stable, dashed for unstable). The blue curves show the maximum value of x for the periodic solutions (stability not indicated). The symbols HB_1 - HB_4 mark the positions of Hopf bifurcations, Hom_1 and Hom_2 represent homoclinic bifurcations of the equilibrium solution, and HPo marks the location of a homoclinic bifurcation of a periodic orbit. (b) Phase portrait for a periodic orbit on the branch arising from HB_1 at a γ value very close to Hom_1. The dot labelled s marks the position of the equilibrium solution. All other symbols and colours (here and in panels (c) and (e)) are as for Fig. 2. (c) Phase portrait for a periodic orbit on the branch arising from HB_2 at a γ value very close to Hom_2. The dot labelled fs marks the position of a folded singularity. (d) The black curve shows a time series for a periodic orbit on the branch arising from HB_3 at a γ value very close to HPo. The red curve shows a time series for the periodic orbit on the branch arising from HB_2 at the same value of γ. (e) Phase portrait showing the periodic orbits plotted in black and red in (d). (f) Enlargement of part of panel (a) showing more detail of the branch of periodic orbits arising from HB_4; this branch terminates in a homoclinic bifurcation of an equilibrium at Hom_4.

and z-coordinates

$$z_{L^\pm} = -c_1 a_3 x_{L^\pm}^3 + (b_2 + c_1 a_2) c_1 a_3 x_{L^\pm}^2 - (b_1 + c_1 a_1) c_1 a_3 x_{L^\pm} + (c_0 - c_1 a_0).$$

These folded singularities correspond to points where $\mathscr{S}_0$ intersects the fold lines L^- and L^+; for the parameter values given in Table 1, $x_{L^+} = 0.65$ and $x_{L^-} = 0.2$. As already mentioned, folded singularities do not correspond to true singularities of the full system, but (x_{L^+}, z_{L^+}), the folded singularity at $x = 0.65$, turns out to be very important for the onset of spiking in our model, as will be discussed in Section 4.1.

The bifurcation diagram for equations (10) is shown in Fig. 4. The branch of ordinary singularities changes stability at the Hopf bifurcations marked HB_3 and HB_4. These are singular Hopf bifurcations resulting from the z-nullcline crossing the folds of $\mathscr{S}_0$. As expected from GSPT, these Hopf bifurcations persist in the full system, becoming HB_3 and HB_4 in Fig. 3(a), at parameter values close to the corresponding values in Fig. 4. In equations (10) and Fig. 4, the branches of periodic orbits arising from HB_3 and HB_4 both terminate at homoclinic bifurcations when they collide with a saddle-type folded singularity. These homoclinic bifurcations are replaced by much more complicated sequences of bifurcations in the full system, as seen in Fig. 3(a) and (f). For later reference, we note that for $\gamma > x_{L^+} = 0.65$, (x_{L^+}, z_{L^+}) is a saddle point of (10), with eigenvalues approximately given by $\lambda_1 = 2.4\varepsilon(\gamma - 0.65)$ and $\lambda_2 = -2.25 - \lambda_1$.

The stability of the branch of ordinary singularities of (10) also changes at two transcritical bifurcations, denoted T_1 and T_2 in Fig. 4, that occur when the branch crosses the branches of folded singularities. These bifurcations become singular Hopf bifurcations in the full model, denoted HB_1 and HB_2 in Fig. 3(a), and are associated with the z-nullcline crossing the folds of S_0. We have checked that as δ gets smaller, the bifurcating branches of periodic orbits in the full model get steeper, as expected for singular Hopf bifurcations.

4 Spike-adding transitions

As shown in Fig. 1, system (1) with parameter values as in Table 1 has bursting solutions for some choices of γ. The solution shown in Fig. 1 has five spikes per burst, but this number can change as γ or other parameters are varied. We are interested in the mechanisms by which spikes may be added or subtracted as parameters are varied. In this section, we discuss two types of spike-adding transitions, one in which three different time scales are important in the addition of a single spike and one in which only two time scales play a significant role.

First, we clarify what we mean by *spike* in the context of system (1), and give the criterion we use to decide when a new spike has been added. We define a spike as an oscillation that is part of a periodic attractor of the system and contains two segments on the fastest time scale. Hence, spikes correspond to orbit segments that follow both attracting sheets of S_0. With this definition, folded-saddle canards with head qualify as spikes even though they exist only in a narrow parameter interval. Similarly, relaxation oscillations preceded by a superslow canard segment, as shown in Fig. 6, panel 11, also fit our definition of a spike, but are also short-lived configurations. We are interested in the appearance of fully developed, robust spikes, i.e., relaxation oscillations without superslow canard segments, as shown in Fig. 6, panel 12. In our system, such

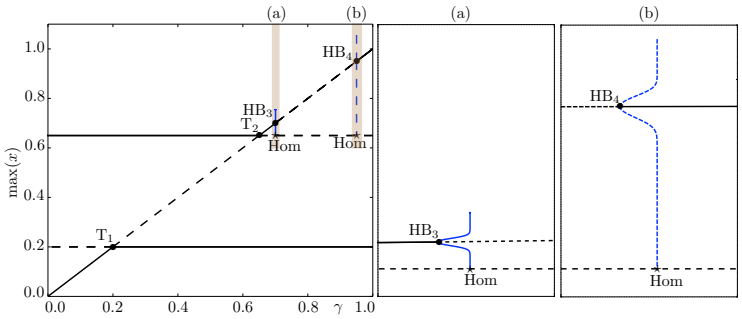

Figure 4: The bifurcation diagram for system (10) is shown in the left panel. The diagonal line shows a branch of ordinary singularities (solid for stable, dashed for unstable). The two horizontal lines indicate branches of folded singularities (solid for stable, dashed for unstable). The ordinary and folded singularities intersect at transcritical bifurcations labelled T_1 and T_2. The near vertical curves (blue) indicate maximum and minimum x values on two branches of periodic solutions (both branches unstable), with each branch arising from a Hopf bifurcation (HB) of the ordinary singularity. Enlargements of the shaded parts of the left panel are shown in the right two panels. Each branch of periodic solutions terminates in a homoclinic bifurcation where the branch collides with the folded singularity at $x = 0.65$.

spikes appear very soon after the parameter value at which the periodic orbit contains a maximal folded-saddle canard segment, as in Fig. 6, panel 10. Thus, for our system, a computationally convenient (if approximate) criterion for the moment of addition of a new spike is the point at which the folded-saddle canard segment reaches L^-, i.e., $x = 0.2$.

4.1 Spike adding utilizing three time scales

An example of a spike-adding transition involving three time scales is seen in system (1) with parameter values as in Table 1, and occurs on the branch of periodic solutions arising from the Hopf bifurcation marked HB_4 in Fig. 3(f). The addition of a spike in this regime is a canard-mediated process that involves a canard explosion associated with the slow and superslow time scales as well as canard orbits associated with passage near the folded saddle (x_{L^+}, z_{L^+}). In the following, we describe changes observed as γ decreases from its value just before HB_4 (γ just larger than 0.95) until the value at which the periodic orbit has a single spike (γ just less than 0.95); the addition of the second and subsequent spikes occurs in an analogous way. We note that the equilibrium of system (1) has x-coordinate equal to γ, meaning that its position hardly changes during the first spike-adding transition.

The transition occurs in the following steps, with corresponding phase portraits shown in Figs 5 and 6.

(1) As the equilibrium point crosses T^+, the upper fold point of the superslow manifold $\mathscr{S}_0$, a singular Hopf bifurcation occurs, creating a small canard cycle as seen in Fig. 5, panel 1. The canard cycle contains segments occurring on both the slow and superslow time scales.

(2) The canard cycle grows until it contains a maximal canard, which occurs when one part of it reaches the vicinity of T^-, the lower fold point of $\mathscr{S}_0$; see Fig. 5, panel 2.

(3) The cycle then develops a section along the left attracting branch of $\mathscr{S}_0$, becoming a canard cycle with head; see Fig. 5, panel 3. Up to this point, the canard cycle is essentially two dimensional, since it lies close to S_0, and involves just the slow and superslow time scales.

(4) As γ decreases further, the head of the canard cycle grows until it approaches the vicinity of the folded saddle, marked **fs**, lying at the intersection of $\mathscr{S}_0$ and L^+. Then the slow segment (indicated by the double arrows pointing leftward in Fig. 5, panel 4) follows the true canard of the folded saddle, then flows back to $\mathscr{S}_0$ along the folded saddle's faux canard by spiralling around it; the oscillations around the faux canard are not visible on the scale used in Fig. 5. Note that the amplitude of such oscillations depends on the relative magnitude of the eigenvalues of the folded saddle in the desingularised slow reduced system. More detail about the dynamics near faux canards of folded saddles can be found in [24].

(5) As γ decreases still further, the segment following the folded saddle's true canard will cross L^+. The cycle then becomes properly three dimensional when it develops a fast component that leaves the repelling sheet of S_0 and jumps back to the right attracting sheet of S_0; see Fig. 5, panel 5.

(6) The segment of the cycle on the repelling sheet of S_0 grows as γ decreases until it reaches a length such that the subsequent fast jump lands on the right sheet of S_0 exponentially close to the middle branch of $\mathscr{S}_0$. This allows a second superslow canard segment to appear in the cycle, followed by a jump on the slow time scale towards the left attracting branch of $\mathscr{S}_0$ and an orbit segment moving along the left attracting branch of $\mathscr{S}_0$ towards T^-, as shown in Fig. 5, panel 6.

(7) Further decreasing γ causes the second superslow canard segment on the middle branch of $\mathscr{S}_0$ to grow while the orbit segment on the left attracting branch of $\mathscr{S}_0$ shrinks. Eventually the second superslow canard segment reaches T^+ and becomes maximal, as shown in Fig. 6, panel 7. At this point, the superslow canard segment is followed by a slow jump towards the right attracting branch of $\mathscr{S}_0$.

(8) The second superslow canard then starts to shrink in size; see Fig. 6, panel 8.

(9) When the second superslow canard shrinks to nothing, the cycle no longer has a superslow segment after the fast jump; see Fig. 6, panel 9.

(10) Once the second superslow canard segment has disappeared, the growth of the slow segment along the folded saddle's true canard (on the repelling sheet of S_0) can resume. It grows until it is maximal, which occurs when the segment reaches L^- (see Fig. 6, panel 10).

(11) As γ decreases still further, a fast jump towards the left attracting sheet of S_0 develops at the same time as the orbit segment along the true canard

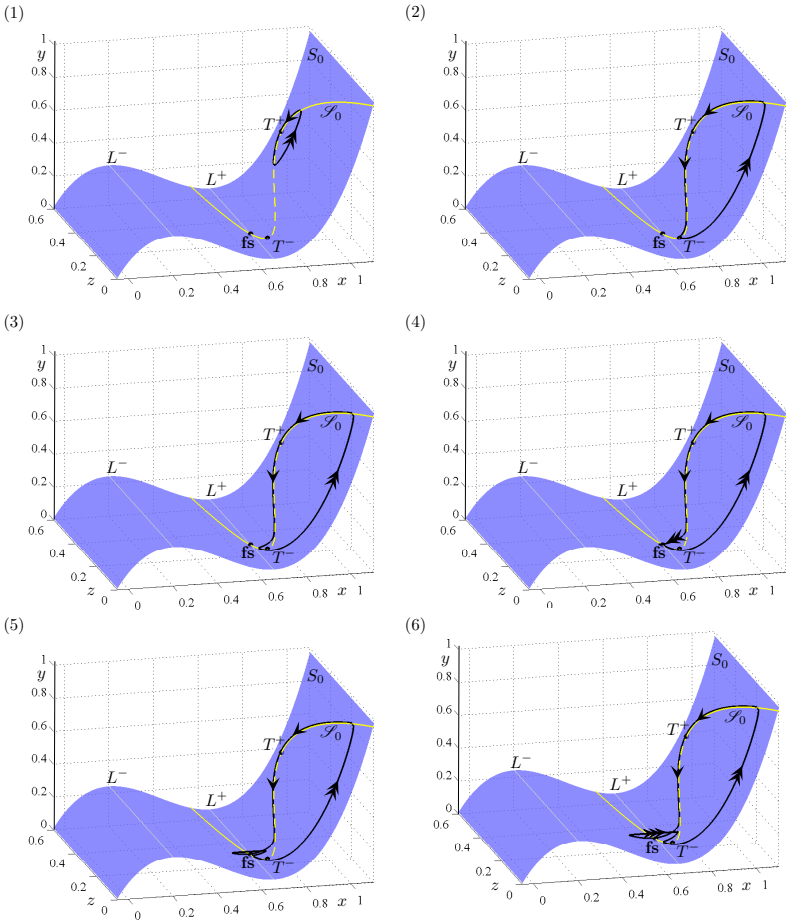

Figure 5: Spike adding in equations (1) with parameter values as in Table 1: steps 1) to 6) in the transition from attracting equilibrium solution to attracting one-spike periodic orbit. In panel 1, $\gamma \approx 0.95012327$; in panels 2 to 6 $\gamma \approx 0.95012344$.

of the folded saddle shrinks. At this point we regard the new spike as having appeared. As γ decreases more, the orbit segment along the true canard disappears completely; see Fig. 6, panel 11.

(12) Once the orbit segment along the true canard has gone, the first superslow canard segment starts to reduce in length and the fast segment from L^- to the right attracting sheet of S_0 moves to larger values of z. Eventually, this fast segment has a landing point on S_0 exponentially close to the middle repelling branch of $\mathscr{S}_0$. After this, the development of another superslow canard segment is possible, resulting in an orbit with one spike and two superslow canard segments as shown in Fig. 6, panel 12. If γ decreases still further, the formation of a second spike begins, with the transition being analogous to steps 2 to 12 described above.

As is clear from the description above, steps 1 to 3 in this transition involve

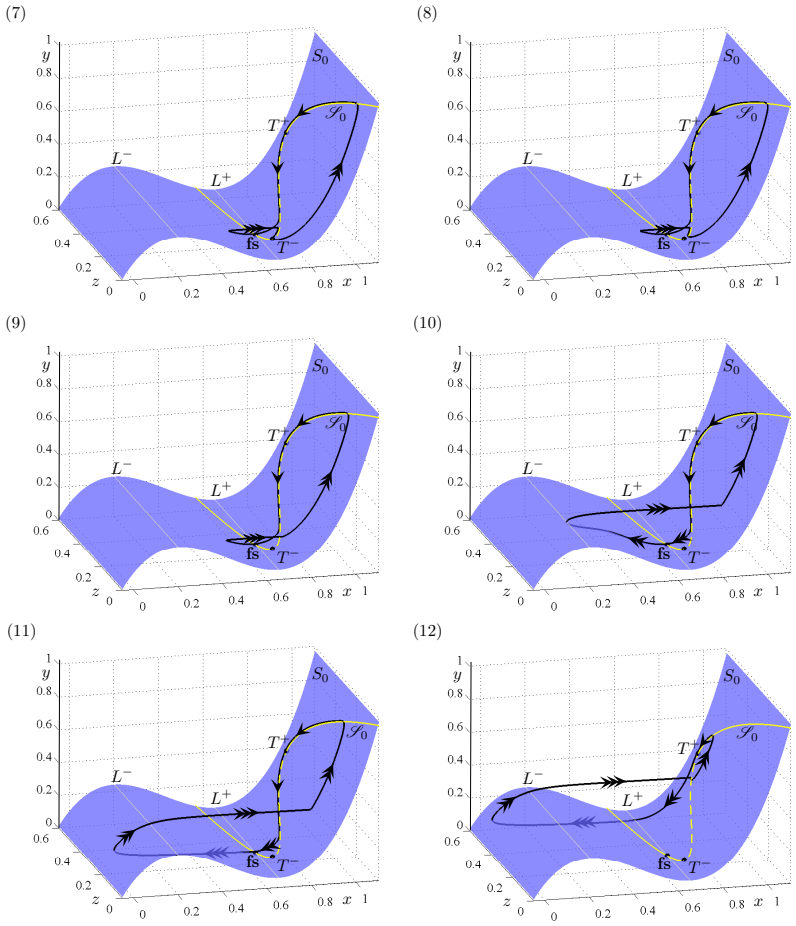

Figure 6: Spike adding in equations (1) with parameter values as in Table 1: steps 7) to 12). In panels 7 to 10 $\gamma \approx 0.95012344$; in panel 11 $\gamma \approx 0.94905122$; in panel 12 $\gamma \approx 0.94883380$.

the slow and superslow time scales only, and are analogous to canard explosions seen commonly in two-time-scale systems. The fast time scale becomes important for the transition when the cycle gets close to the folded-saddle singularity in step 4, and all three time scales are involved in the changes that occur in steps 4 and 5. From step 5 onward, the cycle continues to have segments on all three time scales, but the significant changes that occur in steps 5 to 9 again just involve the slow and superslow time scales. In steps 10 to 12, the superslow time scale is not involved in the main changes described above; its role in spike-adding only resumes when the transition from one to two spikes starts after step 12.

We note that the interaction between a limit cycle and a folded saddle, as occurs in step 4, was studied in [8]. This interaction has a corresponding bifurcation in the desingularised slow reduced system (10), specifically where a homoclinic bifurcation ends the branch born at HB_4; see Fig. 4 (b). This phenomenon was called a *folded homoclinic connection* in [8], and organises in

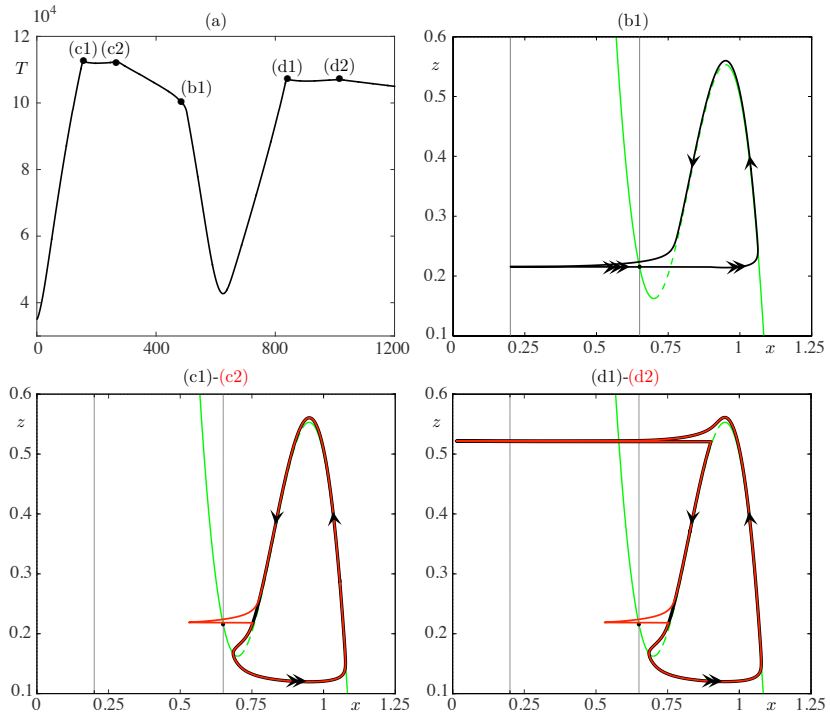

Figure 7: Period and phase portraits for orbits on the spike-adding branch emanating from HB_4. (a) Period of the orbit plotted as a function of the numerical step along the branch: point 0 on the x-axis corresponds to $\gamma = 0.95004655032$ while point 1200 corresponds to $\gamma = 0.94883293533$. This choice of x-axis scaling allows the critical points of the period to be distinguished. (b) Projection onto the $x - z$ plane of the orbit corresponding to point (b1) in panel (a); this corresponds to the orbit in Fig. 5, panel 10. In this and the following panels, the green curve is the projection of $\mathscr{S}_0$ and the grey vertical lines are the projections of L^+ and L^-. (c) Projection onto the $x - z$ plane of the orbits corresponding to points (c1) (black curve) and (c2) (red curve) in panel (a); these correspond to the orbits in Fig. 5, panel 2 and Fig. 6, panel 7, resp. (d) Projection onto the $x - z$ plane of the orbits corresponding to points (d1) (black curve) and (d2) (red curve) in panel (a).

the full system the transition from cycles evolving on the superslow/slow time scale to cycles with spikes.

The description of the spike adding given above focussed on the major geometric changes associated with the transition. In addition to the changes described, the branch of limit cycles undergoes several secondary bifurcations (e.g., folds, period doubling bifurcations, possibly one or more secondary Hopf bifurcations producing a torus) and special intermediate cycles containing canard segments are encountered, but we do not discuss these bifurcations further since they are not important for the spike-adding phenomenon of interest here.

In computational work on spike adding in two-time-scale systems, it is common to identify the moment of spike adding with the parameter value at which

the period of the canard cycle has a local maximum [27]. This identification arises from recognising that the time spent on a canard segment increases as the length of the canard segment increases, then decreases once the maximal canard has been passed. Since a new spike is typically observed exponentially close to the parameter value at which the maximal canard occurs, it is convenient from a computational point of view to say that the spike adding occurs at the point of maximum period. Similar considerations are also important in spike adding in three-time-scale contexts, but there are added complications. In particular, there are several stages in the spike adding shown in Fig. 5 and Fig. 6 at which there are maximal canards, namely at the parameter values for the orbits shown in panels 2, 7 and 10 of these figures. The first two of these correspond to maximum length of a (superslow) canard segment on the repelling branch of $\mathscr{S}_0$ while the third corresponds to maximum length of a (slow) canard segment on the repelling branch of S_0.

The maximal canard shown in Fig. 6, panel 10 is maximal with respect to the repelling slow manifold (which is a perturbation of the middle sheet of S_0) and is associated with the folded-saddle singularity **fs**. As discussed above, we identify this transition cycle with the moment of addition of a spike in the system, upon variation of γ. However, as can be seen in Fig. 7(a), this cycle is not associated with a maximum of the period of the cycle; the cycle shown in Fig. 6, panel 10 corresponds to the point labeled (b1) in Fig. 7(a). Instead, there are two local maxima before the spike appears, labelled (c1) and (c2) in Fig. 7(a); these correspond to the maximal canards shown in Fig. 5, panel 2 and Fig. 6, panel 10, resp. In addition, there are a further two local maxima of the period at parameter values after the spike has been added; these are labelled (d1) and (d2) in Fig. 7(a), and correspond to maximal canards analogous to (c1) and (c2) occurring during the transition in which a second spike is being added.

The reason why cycles containing maximal folded-saddle canard segments do not correspond, in this system, to local maxima of the period function can be understood by looking at the specific geometry in our system. As the maximal folded-saddle canard is approached (moving from panel 9 to 10 in Fig. 6) the slow segment following the true canard of the folded saddle gets longer, but this results in a shorter slow segment near the right attracting sheet of S_0. Since the extra time spent on the former slow segment does not compensate for the time lost from the latter one, cycles that spend more time near the true canard of the folded saddle end up having a smaller total period.

This observation that the lengths of canard segments on the superslow manifold have a stronger influence on the period of the cycle than the lengths of any canard segments that are on the slow manifold but not on the superslow manifold is likely to be true for any three time scale system. This means that locating spike adding by identifying parameter values for which there is maximum period may be problematic in three-time-scale systems, and strategies that involving inspection of phase portraits are advisable.

4.2 Spike adding utilizing two time scales

Spike adding like that seen in Figs 5 and 6 can only happen if the fast return segment (from the vicinity of the repelling sheet of S_0 to the right attracting sheet of S_0) gets sufficiently close to the repelling branch of $\mathscr{S}_0$. If the return

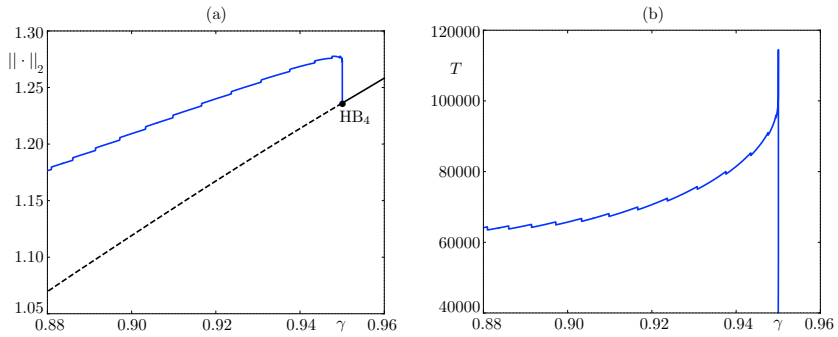

Figure 8: (a) Partial bifurcation diagram for equations (14) with γ varying, for $\alpha_2 = 0.6$ and all other parameter values as in Table 3. The black curve represents equilibrium solutions (solid for stable, dashed for unstable). The blue curve shows the L_2-norm of the periodic solution created in the Hopf bifurcation at HB$_4$. (b) Period as a function of γ along the branch of limit cycles shown in panel (a).

segment does not get close enough to the repelling branch, the steps associated with the existence of a second superslow canard segment (i.e., steps 6 to 8 in Figs 5 and 6) will be omitted. In this case, the addition of a new spike involves the interaction of two time scales only, and is associated with passage near the folded saddle.

Using the alternative parametrization of system (1) given in the Appendix, it is straightforward to check that varying α_2 will change the distance between $\mathscr{S}_0$ and the position where the fast return segment hits S_0 while leaving unaltered the basic bifurcation structure shown in Fig. 3(a). In particular, we have checked that changing α_2 does not affect the branch of equilibria shown in Fig. 3(a) or the number of Hopf bifurcations, although the nature of the branches of periodic orbits emanating from the different Hopf bifurcations can change. For instance, when $\alpha_2 = 0.6$ the branch of periodic orbits arising from HB$_1$ terminates at HB$_2$, whereas for $\alpha_2 = 0.65$ the branches from these two Hopf bifurcations both terminate at homoclinic bifurcations.

We focus here on the case $\alpha_2 = 0.6$, with other parameters as before; note that the parameter values considered until now, including for construction of Figs 5 and 6, correspond to the choice $\alpha_2 = 0.65$. We are interested in the spike-adding branch that arises from HB$_4$, which is shown in part in Fig. 8(a). Note that this panel uses the L$_2$-norm as solution measure along the branch of limit cycles, unlike in Fig. 3(f), since this allows the spike-adding transitions to be more easily distinguished. Comparison of Fig. 8(a) and Fig. 3(f) suggests that a different spike-adding mechanism might be in operation for the two cases, and this is indeed so. In particular, the main steps in the first spike-adding transition for this branch, as γ decreases, are as follows:

(1) Steps 1 to 5 occur just as before. That is, a small canard cycle appears in the Hopf bifurcation at HB$_4$, grows in amplitude until there is a maximal canard segment on the middle branch of $\mathscr{S}_0$, then becomes a canard cycle with head, and eventually enters the vicinity of the folded saddle, f_s, as shown in Fig. 9, panel 1. The cycle then interacts with the true and faux

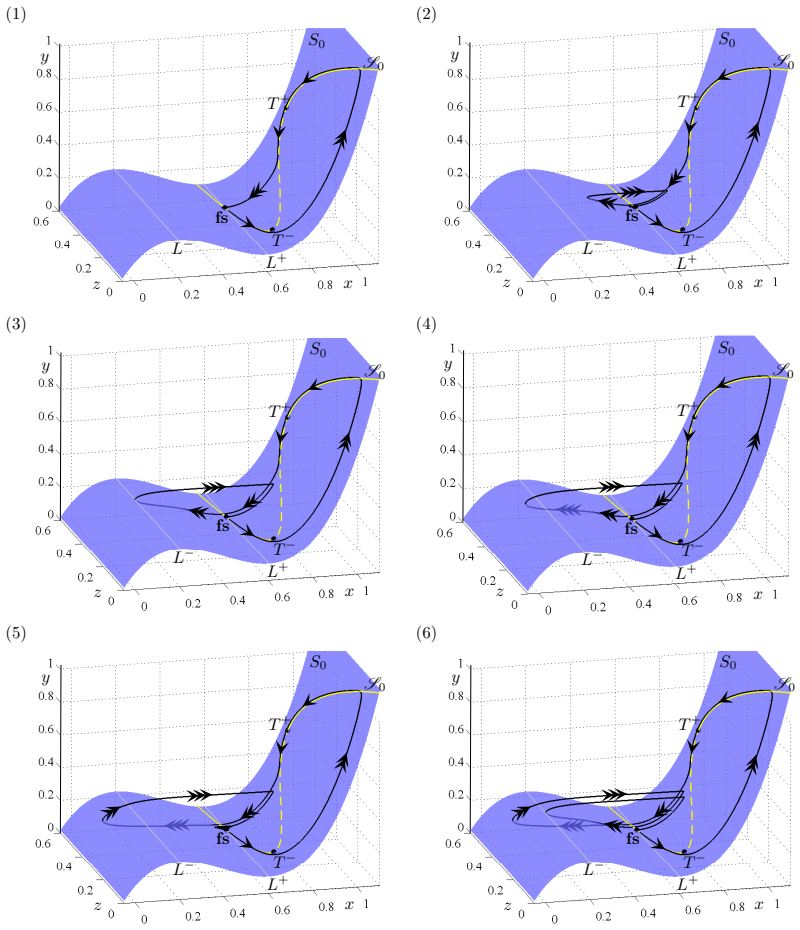

Figure 9: Spike adding in equations (14) for $\alpha_2 = 0.6$ and all other parameter values as in Table 3. In panel 1 $\gamma \approx 0.95003602$; in panel 2 $\gamma \approx 0.95003601$; in panels 3 and 4 $\gamma \approx 0.95003596$; in panel 5 $\gamma \approx 0.95003533$; in panel 6 $\gamma \approx 0.95003509$.

canards of the folded saddle, as described for Step 4 in the previous case, and eventually crosses L^+ and develops a fast return segment from the repelling sheet of S_0 to the right attracting sheet of S_0; see Fig. 9, panel 2. Note that the fast return segment lands on the right sheet of S_0 well below the middle branch of $\mathscr{S}_0$.

(2) As γ decreases further, the canard segment on the repelling middle sheet of S_0 grows, becoming maximal when it extends all the way to L^-; see Fig. 9, panel 3. Unlike the case for $\alpha_2 = 0.65$, at no stage during the growth of this canard segment does the fast return segment get close to the middle branch of $\mathscr{S}_0$, with the consequence that Steps 6 to 8 of the earlier spike-adding transition are missing. Comparison of Fig. 9, panel 3 and Fig. 6, panel 10 highlights another important difference for the case with $\alpha_2 = 0.6$, i.e., at all γ values the fast return segment returns to S_0

on the high-z side of $\mathscr{S}_0$, meaning that the cycle has a second superslow segment as it travels along $\mathscr{S}_0$ from the folded saddle to T^- before making a slow jump to the right attracting branch of $\mathscr{S}_0$. By comparison, at the analogous stage of spike adding when $\alpha = 0.65$, the fast segment is followed directly by a slow jump to the right attracting branch of $\mathscr{S}_0$ or by an excursion near the middle branch of $\mathscr{S}_0$ and then a slow jump to the right branch of $\mathscr{S}_0$.

(3) Once the configuration shown in Fig. 9, panel 3 has been reached, we consider that a new spike has been added. The process continues as for the previous case, with the development of a canard with head (Fig. 9, panel 4) until the point where the slow canard disappears completely and a full relaxation oscillation is present (Fig. 9, panel 5). We note that the cycle shown in Fig. 9, panel 5 passes close to the faux canard of the folded saddle, and small oscillations seen as it does so are oscillations of the orbit around the faux canard; see [24] for further details about this kind of dynamics.

(4) As γ is decreased still further, extra spikes are added to the orbit in an analogous manner to that described above. Fig. 9, panel 6 shows the moment of addition of the second spike, when there is again a maximal slow canard on S_0 analogous to the situation shown in Fig. 9, panel 3.

A crucial difference between the spike-adding mechanism described in this section and the mechanism described in Section 4.1 lies in the time scales that are involved. In the spike adding shown in Fig. 9, once the folded saddle has been encountered for the first time (Fig. 9, panel 1), additional orbit segments that appear are associated with motion on the slow or fast time scales. By comparison, the spike adding shown in Figs 5 and 6 requires the addition of orbit segments evolving on the superslow time scale as well. A consequence of the absence of superslow canard transitions in the spike adding in the scenario described in this section is that the addition of a new spike corresponds to a local maximum of the period, and this property can be used to detect the spike adding numerically; see Fig. 8 (b) for an illustration of this aspect.

Overall, the folded-saddle spike adding mechanism present in this configuration of our model is reminiscent of what happens in other two-time-scale spike-adding scenarios, in particular in parabolic bursting [8] where the addition of a new spike exclusively results from a passage near the true canard associated with the folded-saddle singularity. Similar to what has been reported in the context of parabolic bursting models, we have found homoclinic bifurcations in the DSRS (see Fig. 4); these are referred to as folded homoclinic bifurcations in [8].

5 Conclusions and discussion

In this work, we have analysed the role of time scales in shaping and organising families of bursting limit cycles in a three-dimensional, three-time-scale model. This model is phenomenological although its development was motivated by an attempt to understand some features of secretory neural activity [25]. The minimal number of state variables, minimal nonlinearities and numerous parameters

make this model a prototypical three-time-scale burster whose flexibility makes it particularly amenable to analysis and computations.

The bursting dynamics that we report, and of which we provide initial analysis in this work, is shaped through the interaction between a two-dimensional cubic-shaped critical manifold S_0 (and its associated two-dimensional attracting and repelling Fenichel slow manifolds) and a one-dimensional cubic-shaped superslow manifold $\mathscr{S}_0$ (and its associated one-dimensional attracting and repelling Fenichel superslow manifolds). With parameter values chosen as in [25], the typical bursting dynamics generated by this model can be described as follows. The quiescent phase of the bursting cycle evolves on two time scales: it follows the attracting branches of $\mathscr{S}_0$, the relevant parts of which lie on an attracting sheet of S_0, on the superslow time scale; as it reaches the fold points of $\mathscr{S}_0$, it stays near the same attracting sheet of S_0 and flows along it on the slow time scale. The subsequent active phase is formed by one or more relaxation oscillations comprised in a classical way from two slow segments along attracting sheets of S_0 and two fast jumps from a fold line of S_0 to the opposite attracting sheet. Overall, therefore, there are three time scales evident in one bursting cycle.

The configuration described above corresponds to robust bursting cycles that occur in our model for the parameter values originally specified in [25], as shown in Fig. 2. In parameter space, these cycles are generated through a Hopf bifurcation that initially creates small spikeless periodic solutions, which then grow spikes one by one along a continuous branch. In this work, we have identified the many steps by which this happens. In particular, we have shown that two types of canard contribute to the spike-adding transitions: superslow canards that occur on the attracting and repelling branches of $\mathscr{S}_0$, and slow canards that lie on attracting and repelling sheets of S_0. For this choice of parameters, we have shown that there are multiple superslow canard explosions resulting from the possible proximity of the return point of the last spike of the burst and $\mathscr{S}_0$, as shown in Figs 5 and 6. We have also shown that the presence of a folded saddle has a significant effect on the spike adding.

We then investigated an effect on the full system's dynamics of shifting the position of $\mathscr{S}_0$ relative to S_0. We showed that a small change in one parameter, which alters the height of one fold of S_0 relative to the position of $\mathscr{S}_0$, was sufficient to significantly change the spike-adding process. Specifically, the change in geometry resulted in the return point on S_0 of the last spike in a burst being shifted away from $\mathscr{S}_0$, thereby preventing the occurrence of multiple superslow canard explosions. This simplified the spike-adding transition by removing some of the steps (see Fig. 9) and resulted in the occurrence of smaller quasi-vertical segments in the overall bifurcation diagram, as shown in Fig. 8. An important difference between the two types of spike-adding transition we have described is in the number of time scales involved. The first scenario (Figs 5 and 6) involves all three time scales of the problem, but, after the initial phase lasting from the Hopf bifurcation to the first encounter with the folded-saddle singularity, spike adding in the second scenario (Fig. 9) involves the addition of orbit segments evolving on only two different time scales.

In the first scenario, spike adding resulted from passage near both the repelling branch of the one-dimensional superslow manifold $\mathscr{S}_0$ and the repelling sheet of the two-dimensional critical manifold S_0. The former type of passage is organised by canard points, and the latter by folded-saddle singularities. Hence,

to a certain extent, our first scenario for spike-adding transitions resembles a mix of what has been previously seen in three-dimensional square-wave bursters in, e.g., [7, 27, 30], and what has been seen in four-dimensional parabolic bursters in [8]. In particular, the possibility of canard transitions near $\mathscr{S}_0$ when the trajectory returns, after the fast segment of the last spike, to a position near the right attracting sheet of S_0 exponentially close to $\mathscr{S}_0$, is reminiscent of what happens in square-wave bursters. Indeed as explained in e.g. [7, 12], each spike-adding canard transition in a square-wave burster occurs when the trajectory returns, after the fast segment of the last spike, very close to the homoclinic connection of the fast subsystem; this terminates the burst. Since the trajectory is now exponentially close to the one-dimensional slow manifold, it can connect to the slow manifold and develop a new canard segment. The second spike-adding scenario involves only the folded-saddle passage and is, in that respect, closer to spike adding in a parabolic burster. This shows the power of this model since it can display multiple canard-mediated spike-adding scenarios within a minimal three-dimensional setting, at the cost of having one more time scale compared to more classical bursting scenarios.

There is an important difference, from a computational point of view, between the spike-adding in our model and that seen in many two-time-scale models. In particular, the onset of a new spike under the first scenario in our model is not typically associated with a local maximum of the period of the bursting oscillations, unlike the case for two-time-scale spike adding of fold-initiated bursting. This is important computationally, since algorithms for detection of spike-adding commonly detect a turning point in the period as a proxy for onset of spike-adding. Clearly this approach would not be appropriate for detection of spike-adding in three-time-scale systems such as ours. Instead, spike onset was detected in our first scenario by declaring that the maximal folded-saddle canard segment (which in our convention corresponds to the onset of a new spike) is reached when the minimum of variable x along the bursting cycle is equal to $x_{L_-} = 0.2$. This approach is less precise than one that looks for maxima of the period, but gives a good approximation of the maximal folded-saddle canard segment close to the singular limit $\delta = 0$. However, as explained in Section 4.2, with some choices of parameters in our model, the superslow manifold is relatively far from the return point of the fast segment of the bursting cycle, so that the adding scenario is more of a two-time-scale one; in that case the onset of a new spike always corresponds to local maximal of the period function and this can be used to numerically detect the moment of addition of a new spike; see Fig. 8 (b).

The model studied here showcases how three-time-scale systems can display a richer dynamical repertoire than those with two time scales, in particular allowing an interesting interplay between different classical two-time-scale scenarios. In this study we have kept the hierarchy of time scales fixed and have therefore only partially described the possible singular limits. A more thorough and rigorous analysis of the different time scales present in this model, together with a complete investigation of the singular limits associated with equations (1) in all generality, is beyond the scope of the present work and will be an interesting topic for future studies.

Overall, this study adds to the recently growing body of literature on complex oscillations in systems with three time scales [20, 21, 22, 23, 26]. While close in setup to [23], the dynamics analysed here is different due to the presence

of a folded-saddle singularity and not a folded node. The focus is different as well given that we have mostly centred our study on the spike-adding mechanism and the underlying geometry of the slow and superslow manifolds. The model studied here, initially designed in [25], also bears some resemblance to the three-time-scale minimal model from [20], where complicated MMOs were studied; however, the key difference is in the shape of the superslow manifold, which is normally hyperbolic in [20] whereas it has fold points here. In terms of output time series, the dynamics reported here is comparable to that of coupled slow-fast oscillators presented in [22, 26], even though the compact form of the equations here makes this model both dynamically rich and more amenable to analysis and computations. This study can open doors to further work on three-time-scale dynamics, for instance on canard-mediated synchronisation properties of two or more such systems, in light of what was done in, e.g., [17].

Finally, although this model is entirely phenomenological, it is biologically motivated, and the results presented here could shed light on three-time-scale phenomena observed in biophysical models and in experiments. In particular, follow-up work could include using such prototypical models to identify markers of three-time-scale dynamics (in particular in terms of oscillatory patterns, threshold crossings, etc.), both in synthetic and experimental data relevant to neuronal studies.

A Alternative parametrisation of the model

It is sometimes useful to consider equations (1) in the alternative but equivalent form

$$\begin{aligned}
\frac{dx}{dt} &= y - \left(2ax^3 - 3a(\alpha_1+\alpha_2)x^2 + 6a\alpha_1\alpha_2 x + a_0\right)\\
\frac{dy}{dt} &= \delta\left(3b((\beta_1+\beta_2)-(\alpha_1+\alpha_2))x^2 - 6b(\beta_1\beta_2-\alpha_1\alpha_2)x - \frac{b}{a}y - z + \frac{ab_0+a_0b}{a}\right)\\
\frac{dz}{dt} &= \delta\varepsilon(x-\gamma).
\end{aligned} \tag{14}$$

The only difference between systems (1) and (14) is in the coefficients of each term. The relationships between the coefficients in (1) and in (14) are given in Table 2.

Table 2: Coefficients in (1) expressed in terms of coefficients in (14)

a_1	$6a\alpha_1\alpha_2$
a_2	$3a(\alpha_1+\alpha_2)$
a_3	$2a$
b_1	$6b(\beta_1\beta_2-\alpha_1\alpha_2)$
b_2	$3b((\beta_1+\beta_2)-(\alpha_1+\alpha_2))$
c_0	$(ab_0+a_0b)/a$
c_1	b/a

The constants α_1, α_2, β_1 and β_2 in (14) have particular geometric significance: α_1 and α_2 are the x values for the two fold lines for the critical manifold, L^- and L^+, respectively, shown in Fig. 2, and β_1 and β_2 are the x values for the two turning points of the superslow manifold, T^- and T^+, respectively, also shown in Fig. 2. Parametrisation of the model as in (14) thus makes it easy to move the superslow manifold relative to the critical manifold and, hence, easy to explore any resulting effects on the dynamics. The values of the parameters in model (14) corresponding to the choice of constants in Table 1 are shown in Table 3.

Table 3: Default values for the parameters in model (14).

α_1	0.2	α_2	0.65
β_1	0.7	β_2	0.95
a	2.0	b	25.0
a_0	0.1	b_0	26.5
δ	0.001	ε	0.1

Acknowledgments

Part of this work was done during visits by the authors to each other's institution; MD thanks the University of Auckland and VK thanks Inria Sophia Antipolis Méditerranée for their hospitality. Financial support was provided by the Marsden Fund of NZ and the University of Auckland.

References

[1] R. Bertram, M.J. Butte, T. Kiemel and A. Sherman A, *Topological and phenomenological classification of bursting oscillations*, Bulletin of Mathematical Biology, **57**:413-439, 1995.

[2] M. Brøns, K. Bar-Eli, *Canard explosion and excitation in a model of the Belousov-Zhabotinskii reaction*, J. Phys.Chem., **95**:8706-8713, 1991.

[3] B. Deng, *Food chain chaos due to junction-fold point*, Chaos **11**:514-525, 2001.

[4] B. Deng and G. Hines, *Food chain chaos due to Shilnikov's orbit*, Chaos, **12**:533-538, 2002.

[5] B. Deng and G. Hines, *Food chain chaos due to transcritical point*, Chaos, **13**:578-585, 2003.

[6] M. Desroches, J. Guckenheimer, B. Krauskopf, C. Kuehn, H. M. Osinga and M. Wechselberger, *Mixed-mode oscillations with multiple time scales*, SIAM Rev. **54**(2): 211-288, 2012.

[7] M. Desroches, T. J. Kaper, M. Krupa, *Mixed-mode bursting oscillations: Dynamics created by a slow passage through spike-adding canard explosion in a square-wave burster*, Chaos **23**: 046106, 2013.

[8] M. Desroches, M. Krupa and S. Rodrigues, *Spike-adding in parabolic bursters: the role of folded-saddle canards*, Phys. D **331**: 58–70, 2016.

[9] E.J. Doedel, R.C. Paffenroth, A.C. Champneys, T.F. Fairgrieve, Yu.A. Kuznetsov, B.E. Oldeman, B. Sandstede and X.J. Wang, *AUTO-07p: Continuation and Bifurcation Software for Ordinary Differential Equations*, available at `http://cmvl.cs.concordia.ca/auto/`.

[10] F. Dumortier and R. Roussarie, *Canard cycles and center manifolds*, Memoir of the AMS **121**(577), American Mathematical Soc., 1996.

[11] N. Fenichel, *Geometric singular perturbation theory*, J. Diff. Eqn **31**: 53?98, 1979.

[12] J. Guckenheimer and C. Kuehn, *Computing slow manifolds of saddle type*, SIAM J. Appl. Dyn. Syst. **8**: 854–879, 2009.

[13] J. Guckenheimer, *Singular Hopf bifurcation in systems with two slow variables*, SIAM J. Appl. Dyn. Syst. **7**(4): 1355–1377, 2008.

[14] J. L. Hindmarsh and R.M. Rose, *A model of neuronal bursting using three coupled first order differential equations.* Proc. R. Soc. London, Ser. B **221**: 87–102, 1984.

[15] E.M. Izhikevich, *Neural Excitability, Spiking, and Bursting*, International Journal of Bifurcation and Chaos, **10**:1171-1266, 2000.

[16] C. K. R. T Jones, *Geometric Singular Perturbation Theory*, In: *Dynamical Systems*, R. Johnson Ed., Lecture Notes in Mathematics vol. **1609**, Springer-Verlag, Berlin, 1995.

[17] E. Köksal Ersöz, M. Desroches, M. Krupa and F. Clément, *Canard-mediated (de)synchronization in coupled phantom bursters*, SIAM J. Appl. Dyn. Syst. **15**(1): 580–608, 2016.

[18] I. Kosiuk and P. Szmolyan, *Geometric analysis of the Goldbeter minimal model for the embryonic cell cycle*, Journal of Mathematical Biology, **72**:1337-1368, 2016. doi:10.1007/s00285-015-0905-0

[19] M. Krupa and P. Szmolyan, *Extending geometric singular perturbation theory to non-hyperbolic points - fold and canard points in two dimensions*, SIAM J Math Anal **33** :286?314, 2001.

[20] M. Krupa, N. Popovic, and N. Kopell, *Mixed-mode oscillations in three time-scale systems: A prototypical example*, SIAM J. Appl. Dyn. Syst., **7**: 361-420, 2008.

[21] M. Krupa and M. Wechselberger, *Local analysis near a folded saddle-node singularity*, J. Differential Equations **248**(12): 2841–2888.

[22] M. Krupa, A. Vidal, M. Desroches, and F. Clément, *Mixed-mode oscillations in a multiple time scale phantom bursting system*, SIAM J. Appl. Dyn. Syst., **11**:1458-1498, 2012.

[23] B. Letson, J. E. Rubin and T. Vo, *Analysis of interacting local oscillation mechanisms in three-timescale systems*, SIAM J. Appl. Math. **77**(3): 1020–1046, 2017.

[24] J. Mitry and M. Wechselberger, *Folded saddles and faux canards*, SIAM J. Appl. Dyn. Syst., **16**:546-596, 2017.

[25] P. Nan, *Dynamical Systems Analysis of Biophysical Models with Multiple Timescales*, PhD thesis, The University of Auckland, 2014.

[26] P. Nan, Y. Wang, V. Kirk, and J.E. Rubin, *Understanding and distinguishing three-time-scale oscillations: a case study in a coupled Morris-Lecar system*, SIAM J. Appl. Dyn. Syst., **14**:1518-1557, 2015.

[27] J. Nowacki, H. M. Osinga and K. Tsaneva-Atanasova, *Dynamical systems analysis of spike-adding mechanisms in transient bursts*, The Journal of Mathematical Neuroscience **2**: 1–28, 2012.

[28] M. L. Rosenzweig and R. H. MacArthur, *Graphical representation and stability conditions of predator-prey interactions*, The American Naturalist, **97**:209-223, 1963.

[29] P. Szmolyan and M. Wechselberger, *Canards in* $\mathbb{R}^3$, Journal of Differential Equations **177**(2): 419–453, 2001.

[30] D. Terman, *Chaotic spikes arising from a model of bursting in excitable membranes*, SIAM J. Appl. Math. **51**: 1418–1450, 1991.

[31] T. Vo, R. Bertram and M. Wechselberger, *Multiple geometric viewpoints of mixed mode dynamics associated with pseudo-plateau bursting*, SIAM J. Appl. Dyn. Syst., **12**:789-830, 2013.

[32] M. Wechselberger, *Existence and Bifurcation of Canards in* $\mathbb{R}^3$ *in the Case of a Folded Node*, SIAM Journal on Applied Dynamical Systems **4**(1): 101–139, 2005.